ACS OMEGA

http://pubs.acs.org/journal/acsodf

Article

Unraveling the Structure and Properties of Layered and Mixed ReO_3–WO_3 Thin Films Deposited by Reactive DC Magnetron Sputtering

Boris Polyakov,* Edgars Butanovs, Andrejs Ogurcovs, Anatolijs Sarakovskis, Martins Zubkins, Liga Bikse, Jevgenijs Gabrusenoks, Sergei Vlassov, Alexei Kuzmin, and Juris Purans

Cite This: *ACS Omega* 2022, 7, 1827–1837

Read Online

ACCESS | Metrics & More | Article Recommendations | Supporting Information

ABSTRACT: Tungsten trioxide (WO_3) is a well-known electrochromic material with a wide band gap, while rhenium trioxide (ReO_3) is a "covalent metal" with an electrical conductivity comparable to that of pure metals. Since both WO_3 and ReO_3 oxides have perovskite-type structures, the formation of their solid solutions (ReO_3–WO_3 or $Re_xW_{1-x}O_3$) can be expected, which may be of significant academic and industrial interest. In this study, layered WO_3/ReO_3, ReO_3/WO_3, and mixed ReO_3–WO_3 thin films were produced by reactive DC magnetron sputtering and subsequent annealing in air at 450 °C. The structure and properties of the films were characterized by X-ray diffraction, optical spectroscopy, Hall conductivity measurements, conductive atomic force microscopy, scanning and transmission electron microscopy, energy-dispersive X-ray spectroscopy, and X-ray photoemission spectroscopy. First-principles density functional theory calculations were performed for selected compositions of $Re_xW_{1-x}O_3$ solid solutions to model their crystallographic structure and electronic properties. The calculations predict metallic conductivity and tetragonal distortion of solid solutions in agreement with the experimental results. In contrast to previously reported methods, our approach allows us to produce the WO_3–ReO_3 alloy with a high Re content (>50%) at moderate temperatures and without the use of high pressures.

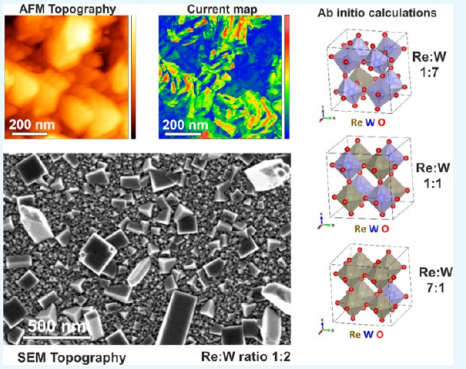

INTRODUCTION

Rhenium trioxide (ReO_3) is a solid material with a perovskite-type cubic crystalline structure that is formed by a network of regular ReO_6 octahedra sharing common vertices in three dimensions with the Re–O–Re angles of 180°.[1] Bulk ReO_3 displays metallic behavior with a specific resistivity in the same range as metallic copper,[2] whereas the resistivity of polycrystalline films ReO_3 is higher ($\rho = 4.0 \times 10^{-3}$ Ωm).[3] ReO_3 can be used as a catalyst in organic synthesis, for example, for amide reduction.[4]

Tungsten trioxide (WO_3) has a perovskite-type monoclinic crystal structure that can be described as a slightly distorted cubic ReO_3-structure, with the corner-shared and tilted WO_6 octahedra.[5] Despite the similarities in the structure, WO_3 is an insulator with electrochromic properties that are successfully utilized in the production of smart windows.[6] Applications in gas sensing were also reported.[7]

Considering that both materials have a perovskite-type structure and close values of ionic radii of Re^{6+} and W^{6+} in ReO_3 and WO_3,[8] it should be possible to form solid solutions of mixed ReO_3–WO_3 (or $Re_xW_{1-x}O_3$) phases with electronic properties different from those of pure WO_3 and ReO_3. Finding a well-controllable method for production of such materials would open the route for tweaking and fine-tuning the characteristics of the ReO_3–WO_3 composite.

WO_3/ReO_3 heterostructures and WO_3–ReO_3 solid solutions were studied theoretically in several works.[9,10] Ling et al. studied the reactivity of hydrogen and methanol on the (001) surfaces of WO_3, ReO_3, WO_3/ReO_3, and ReO_3/WO_3. Additionally, they studied the hypothetical $WReO_6$ structures and found that (001) layered heterostructures are more stable than the mixed ones.[9] Jiang et al. studied coupling between octahedral rotations and local polar displacements in WO_3/ReO_3 superlattices.[10] They found that superlattices with sufficiently thick ReO_3 layers, the absolute number being three or more layers and the rhenium fraction >50%, tend to be more stable than the separated material phases and also show enhanced octahedral rotations in the WO_3 layers.

Received: September 14, 2021
Accepted: December 16, 2021
Published: January 3, 2022

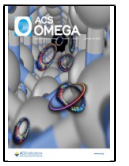

Table 1. Description of Sample Preparation Sequence, Film Thickness, Composition, and Macroscopic Resistivity

sample no.	description of preparation sequence	thickness, nm	resistivity, Ω/sq
1	single layer: amorphous WO_x thin film; annealing: 1 h at 450 °C	WO_3: 120	[a]
2	first layer: amorphous WO_x (100 nm); second layer: amorphous ReO_x (100 nm); annealing: heated for 30 min at 300 °C	WO_3: 125 ReO_3: 100	1.2×10^3
3	first layer: amorphous WO_x (100 nm); second layer: amorphous ReO_x (100 nm); annealing: heated for 30 min at 450 °C	WO_3: 125 ReO_3: 100	1.4×10^5
4	first layer: amorphous ReO_x (100 nm); annealing 1: heated for 30 min at 300 °C second layer: amorphous WO_x (100 nm); annealing 2: heated for 30 min at 450 °C	ReO_3: 135 WO_3: 135	5.3×10^4
5	first layer: amorphous ReO_x (100 nm); second layer: amorphous WO_x (100 nm); annealing: heated for 30 min at 450 °C	ReO_3: 135 WO_3: 135	2.3×10^4
6	simultaneous deposition of ReO_x and WO_x (Re/W ratio 1:7); annealing: heated for 30 min at 450 °C	ReO_3–WO_3: 365	[a]
7	simultaneous deposition of ReO_x and WO_x (Re/W ratio 1:2); annealing: heated for 30 min at 450 °C	ReO_3–WO_3: 500	1.4×10^6
8	simultaneous deposition of ReO_x and WO_x (Re/W ratio 3:1); annealing: heated for 30 min at 450 °C	ReO_3–WO_3: 355	2×10^5

[a]Resistivity is too high to be measured by our system.

However, so far, only two experimental works are available on the synthesis of solid solutions of ReO_3–WO_3.[11,12] The paper by Sleight and Gillson[11] reports the synthesis of WO_3-ReO_3 solid solutions by the method that requires a high pressure (65 kbar) and high temperatures (800–1100 °C). The authors obtained ReO_3–$3WO_3$ crystals with an electrical resistivity of 3.4×10^{-5} Ωm at 25 °C, while the resistivity of pure ReO_3 crystals was 3.6×10^{-7} Ωm. Interestingly, the authors also mention the formation of oxygen-deficient ReO_{3-x} crystalline phases, having the symmetry reduced from cubic to orthorhombic. The second paper by Helbig et al. describes a new organometallic approach to the synthesis of $Re_xW_{1-x}O_3$ phases with up to $x = 0.15$.[12]

In this work, we developed a novel method to produce layered ReO_3/WO_3 and mixed ReO_3–WO_3 thin films by reactive DC magnetron sputtering and subsequent film annealing in air. In contrast to previously reported methods, our method does not require high pressures and allows high ReO_3 content (more than 50%). The crystalline structure of obtained films and their optical and electrical properties were studied by different methods, and the formation of ReO_3–WO_3 solid solutions was proposed. Additionally, first-principles density functional theory (DFT) calculations were performed for selected compositions of $Re_xW_{1-x}O_3$ solid solutions to model their structural and electronic properties. Our theoretical predictions qualitatively agree with the experimental results.

EXPERIMENTAL SECTION

Sample Preparation. Rhenium oxide and tungsten oxide thin films were prepared by reactive DC magnetron sputtering and annealed in air. The targets were a W metal disc (99.9% purity) and a Re metal disc (99.9% purity), which were 50 mm in diameter and 0.3 mm in thickness (GoodFellow). The substrates were 25 × 25 mm fused quartz glasses (SPI Supplies). Magnetron sputtering was performed in the vacuum system SAF25/50 (Sidrabe) at 50–150 W DC magnetron power in a mixed atmosphere of sputtering Ar gas (20 sccm) and reactive O_2 gas (10 sccm) at a total pressure of 20 mTorr. The substrate was mounted 15 cm above the magnetrons and maintained at room temperature during the deposition process.

Eight samples were prepared in total. Sample #1 was prepared by the deposition of the amorphous WO_x film, followed by annealing for 1 h at 450 °C. Samples #2, #3, #4, and #5 had two layers: samples #2 and #3 have WO_x as the first layer, while samples #4 and #5 have ReO_x as the first layer. Sample #2 was prepared by the deposition of the amorphous WO_x film as the first layer and the amorphous ReO_x film as the second layer, following by annealing for 30 min at 300 °C. During annealing, all these and subsequent samples were capped by quartz glass to prevent ReO_3 sublimation. Sample #3 was prepared by the deposition of the amorphous WO_x film as the first layer and the amorphous ReO_x film as the second layer, followed by annealing for 30 min at 450 °C. Sample #4 was prepared by the deposition of the amorphous ReO_x film as the first layer, followed by annealing for 30 min at 300 °C. After deposition of the second layer of amorphous WO_x, the sample was annealed for 30 min at 450 °C. Sample #5 was prepared by the deposition of the amorphous ReO_x film as the first layer and amorphous WO_x of the second layer, followed by annealing for 30 min at 450 °C. Samples #6, #7, and #8 were prepared by simultaneous deposition of WO_x and ReO_x with different Re/W ratios. The fabrication of the samples is summarized in Table 1.

Sample Characterization. The structure and crystallinity of the films were determined by the X-ray diffraction (XRD) technique. The XRD patterns were recorded using a benchtop Rigaku MiniFlex 600 powder diffractometer. Rietveld refinement was performed with BGMN[13] software using the Profex code.[14] The film morphology was studied with a scanning electron microscope SEM/FIB Lyra XM (Tescan). The crystalline structure of the films was imaged using a transmission electron microscope (Tecnai GF20, FEI) operated at a 200 kV accelerating voltage. The electrical parameters were measured in the van der Pauw configuration using a Hall effect system, HMS5000 (Ecopia). Topography and related electric current maps were obtained in the contact mode by an atomic force microscope (AFM) Park NX10 (Park Systems). Optical reflection and transmission spectra were measured using a spectrophotometer Cary 7000 (Agilent). X-ray photoemission spectroscopy (XPS) measurements were performed using an X-ray photoelectron spectrometer ESCALAB Xi (ThermoFisher), and XPSPEAK41 software was used for peak fitting. Raman scattering spectra were recorded in back-scattering geometry using a TriVista777 confocal micro-Raman system (Princeton

https://doi.org/10.1021/acsomega.1c05085
ACS Omega 2022, 7, 1827–1837

Instruments) equipped with an upright Olympus microscope, diode-pumped solid-state laser Cobolt Samba 150 (λ = 532 nm, CW power 150 mW), and an Andor iDus DV420A-OE CCD camera. The laser power at the sample was in the range of 0.46−14.6 mW and controlled by two sets of neutral filters.

First-Principles DFT Calculations. First-principles DFT calculations were performed by the linear combination of atomic orbitals method using the CRYSTAL17 code[15−19] to understand how the cubic structure of pure ReO_3 adopts upon substitution of rhenium atoms with tungsten ones. The calculation details are described in the Supporting Information. The computational scheme was validated using cubic ReO_3 ($Pm\bar{3}m$)[20,21] and several known WO_3 phases.[22−24] A good agreement was found with the available experimental data[20,22−24] and previous first-principles calculations.[25−28] The calculations of mixed ReO_3−WO_3 solid solutions were performed using 2 × 2 × 2 supercells containing eight chemical formulas with removed symmetry and a fully relaxed structure.

RESULTS AND DISCUSSION

X-ray Diffraction Analysis. The X-ray diffraction patterns of WO_3−ReO_3 thin film samples are shown in Figure 1a,b. Their

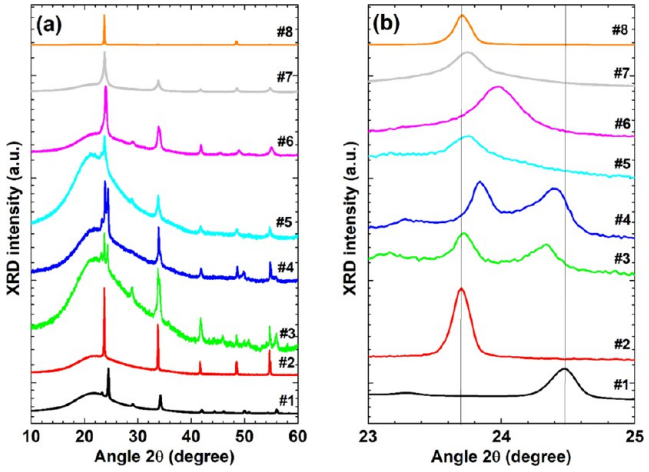

Figure 1. (a) Full spectra of XRD patterns of WO_3 (#1), layered WO_3/ReO_3 (#2, #3), ReO_3/WO_3 (#4, #5), and mixed WO_3−ReO_3 (#6, #7, #8) thin film samples deposited on fused quartz substrates. (b) Zoom-in view of the same spectra in regions 23−25°.

analysis by Rietveld refinement is reported in the Supporting Information, Table S1. The XRD pattern of sample #1 (pure WO_3 thin film) corresponds to the monoclinic ($P2_1/n$) WO_3 phase. Sample #2 has good crystallinity and is composed of a cubic ($Pm\bar{3}m$) ReO_3 phase. A mixture of cubic ReO_3 and monoclinic ($P2_1/n$) WO_3 phases with a reduced crystallite size was found in samples #3 and #4. Samples #5, #6, #7, and #8 correspond to the WO_3−ReO_3 solid solutions, and their XRD patterns were refined using the tetragonal ($P4/nmm$) phase. The reduction of lattice symmetry down to tetragonal is responsible for the appearance of two small peaks at 2θ = 29 and 45°, which are absent in the cubic phase. The smallest crystallite size of about 17−27 nm was found in samples #5, #6, and #7. At the highest rhenium content in sample #8, the crystallite size increases to about 95 nm, and the pattern looks close to that of a cubic ($Pm\bar{3}m$) ReO_3 phase. However, also, in this case, the tetragonal ($P4/nmm$) phase gives a slightly better agreement. The lattice constants of the tetragonal solid solutions with different compositions do not deviate too much and are equal to a = 5.274−5.313 Å and c = 3.748−3.753 Å.

It is interesting to note that samples #2 and #3 have an identical composition after film deposition (WO_3/ReO_3), with the only difference in the annealing temperature (300 °C for sample #2 and 450 °C for sample #3). Only the ReO_3 peaks were visible on the XRD spectrum of sample #2 because the annealing temperature was not sufficiently high to crystallize the amorphous WO_3 layer (Figure 1a,b). While both ReO_3 and WO_3 phases are visible on the XRD spectrum of sample #3. Samples #4 and #5 had a very similar composition (ReO_3/WO_3) but different XRD patterns (Figure 1a,b). In sample #4, the rhenium oxide layer was crystallized and converted into ReO_3 before deposition of the upper WO_3 layer; while in sample #5, the rhenium oxide layer was amorphous before deposition of the upper WO_3 layer. Rietveld analysis of XRD spectra of sample #4 reveals two separate cubic ReO_3 and monoclinic WO_3 phases, while the spectra of sample #5 show a single tetragonal phase attributed to the $Re_xW_{1-x}O_3$ solid solution (Table 2). We explain the different behavior of these samples during the annealing process by higher volatility of amorphous rhenium oxide and the ability to interact with amorphous WO_3 in comparison to crystalline ReO_3.

Transmission Electron Microscopy. For investigation of the thin-film morphology in cross sections, transmission electron microscopy (TEM) lamellas were prepared using focused ion beam scanning electron microscopy (SEM-FIB) and are shown in Figure S3 (Supporting Information). TEM was used to determine the thickness of thin film layers (Table 1) and to investigate the degree of crystallinity of obtained samples. At the cross section of samples #2 and #3, one can see the bottom WO_3 layer and upper ReO_3 layer (Figure S3b,c). For samples #4 and #5, ReO_3 is the bottom layer and empty lacunas can be seen on both samples in Figure S3d,e, while the upper WO_3 layer remains compact. Lacunas are formed due to sublimation and diffusion of rhenium oxide. For mixed WO_3−ReO_3 samples #6, #7, and #8, the film material is homogeneous (Figure S3f,g,h). The most important information about mixed samples #6, #7, and #8 is the high degree of crystallinity of these films. The crystallographic phase of these mixed ReO_3−WO_3 samples was identified as tetragonal $P4/nmm$ and interpreted as $Re_xW_{1-x}O_3$ solid solution (Table 2). At high magnification TEM images, one can see crystallites and atomic structure of samples #6, #7, and #8 (Figure 2). The biggest crystallite size among mixed ReO_3−WO_3 samples demonstrate sample #8, which well corresponds with Rietveld analysis (Table 2).

Optical Properties. Sample #1 (pure WO_3 thin film) was highly transparent similar to other works (Figure 3a).[29,30] All other samples containing rhenium (samples #2−8) were significantly less transparent in comparison to pure WO_3. Their transparency is reversely correlated with the Re content, with a maximal transmittance window in the region around 500 nm (Figure 3b). Visually, all samples containing Re were green-blue in transmitted light (Supporting Information, Figure S1). Maximum transparency of Re-containing samples is close to the transparency window of pure ReO_3, which is in the spectral range of 475−525 nm (Figure S2 in the Supporting Information).[3] In spite of the same composition, sample #3 is more transparent in comparison to sample #2 due to partial sublimation of rhenium oxide. The spectrum of sample #5 is shifted a bit to shorter wavelength in comparison to the spectrum of sample #4. The transmittance window for the spectra of samples #6, #7, and #8 is shifted to shorter

https://doi.org/10.1021/acsomega.1c05085
ACS Omega 2022, 7, 1827−1837

Table 2. Rietveld Analysis of the XRD Patterns of WO_3 and Mixed ReO_3–WO_3 Thin Films[a]

sample no.	phase 1	phase 2
1		100% WO_3 $P2_1/n$ monoclinic a = 7.322 ± 0.001 Å b = 7.544 ± 0.002 Å c = 7.682 ± 0.002 Å d = 66 ± 3 nm
2	100% ReO_3 $Pm\bar{3}m$ cubic a = 3.7508 ± 0.0001 Å d = 464 ± 30 nm	
3	25% ReO_3 $Pm\bar{3}m$ cubic a = 3.7506 ± 0.0002 Å d = 129 ± 10 nm	75% WO_3 $P2_1/n$ monoclinic a = 7.319 ± 0.001 Å b = 7.500 ± 0.002 Å c = 7.680 ± 0.002 Å d = 42 ± 4 nm
4	43% ReO_3 $Pm\bar{3}m$ cubic a = 3.7515 ± 0.0002 Å d = 118 ± 6 nm	57% WO_3 $P2_1/n$ monoclinic a = 7.346 ± 0.001 Å b = 7.615 ± 0.002 Å c = 7.666 ± 0.002 Å d = 42 ± 3 nm
5	100% $Re_xW_{1-x}O_3$ $P4/nmm$ tetragonal a = 5.305 ± 0.002 Å c = 3.753 ± 0.004 Å d = 20 ± 2 nm	
6	100% $Re_xW_{1-x}O3$ $P4/nmm$ tetragonal a = 5.274 ± 0.001 Å c = 3.794 ± 0.001 Å d = 27 ± 2 nm	
7	100% $Re_xW_{1-x}O_3$ $P4/nmm$ tetragonal a = 5.302 ± 0.001 Å c = 3.748 ± 0.002 Å d = 17 ± 2 nm	
8	100% $Re_xW_{1-x}O_3$ $P4/nmm$ tetragonal a = 5.313 ± 0.003 Å c = 3.756 ± 0.002 Å d = 95 ± 2 nm	

[a]Space group, lattice parameters (a,b,c), and the crystallite size (d) are reported.

wavelength; transmittance is reversely correlated with the Re content (Re/W ratio for sample #6, #7, #8 is 1:7, 1:2, 3:1).

Raman Spectroscopy. Raman scattering spectra of WO_3–ReO_3 thin film samples are reported in Figure 4. The appearance of the crystalline WO_3 phase in the as-prepared films depends on the heat treatment process used during their preparation (Figure 4). The metallic layer of cubic ReO_3 located at the top of samples #1 and #2 screens the Raman signal from the bottom WO_3 phase, which is crystalline in sample #1 but amorphous in sample #2. The strong Raman signal in sample #3 is due to the crystallized WO_3 phase (a set of sharp bands at about 132, 270, 328, 607, 714, and 806 cm^{-1} are attributed to the triclinic WO_3 δ-phase[31,32]), while rhenium oxide was evaporated from the sample surface upon heating at 450 °C. In samples #4 and #5, the top layer of tungsten trioxide protects the rhenium oxide sublayer from evaporation. Their Raman spectra are similar and include three main broad bands at 400–500, 500–850, and 850–1050 cm^{-1} additionally to a weak band from the WO_3 phase at about 800 cm^{-1}. The latter disappears in the mixed samples #6, #7, and #8, while the three broad bands remain clearly visible. Note that the intensity of the three broad bands is reduced in samples #7 and #8.

Since cubic ReO_3 shows no or weak Raman activity,[33] the observed sharp peaks in all Raman spectra are related to the WO_3 phase. However, the three broad bands at 400–500, 500–850, and about 950 cm^{-1} in samples #4–#8 are attributed to the WO_3–ReO_3 solid solutions with a tetragonal lattice, which are formed in the films according to our XRD data (Figure 1). Note that the broad band at 950 cm^{-1} is well observed in the as-prepared samples #4, #5, and #6 but is weaker in samples #7 and #8 with a lower tungsten content. In the literature on different tungsten oxide phases, the origin of this band is usually attributed to the presence of the W═O double bonds. In crystalline tungsten trioxide hydrates, the band at about 950 cm^{-1} appears as a relatively sharp peak and is ascribed to the stretching mode of the terminal W═O double bond.[34] In amorphous tungsten oxide thin films, the band at about 950 cm^{-1} has been studied in the past by many authors and is also attributed to the W═O stretching mode.[35−38] At the same time, a weak band located at close wavenumbers was found in ground WO_3 powders and WO_3–ReO_2 mixtures,[39] where it was attributed to reduced tungsten ions $W^{(6-x)+}$ making tungsten–oxygen bonds at the oxide surface or the interface between WO_3 and ReO_2 phases.

We do not expect to have a significant amount (if any) of W═O bonds in our samples of WO_3–ReO_3 solid solutions. Note that the Raman spectrum of sample #6 is similar to that of the tungsten oxide sample studied in ref 40 and attributed to the cubic c-WO_3 phase produced by the low-temperature (around 250 °C) decomposition of $WO_3 \cdot 2H_2O$. However, it is possible that the cubic c-WO_3 phase in ref 40 is indeed tetragonal and was misinterpreted due to the low quality of its XRD pattern.

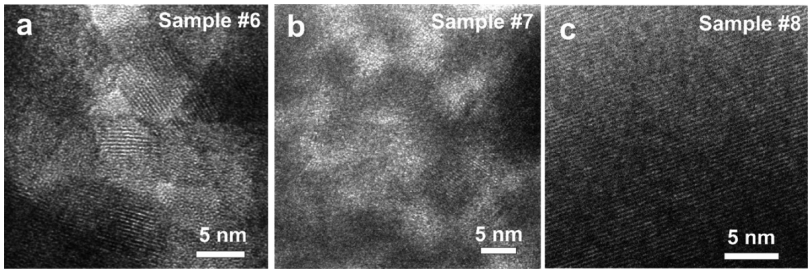

Figure 2. High-magnification TEM images of samples #6 (a), #7 (b), and #8 (c) with a visible atomic structure.

https://doi.org/10.1021/acsomega.1c05085
ACS Omega 2022, 7, 1827−1837

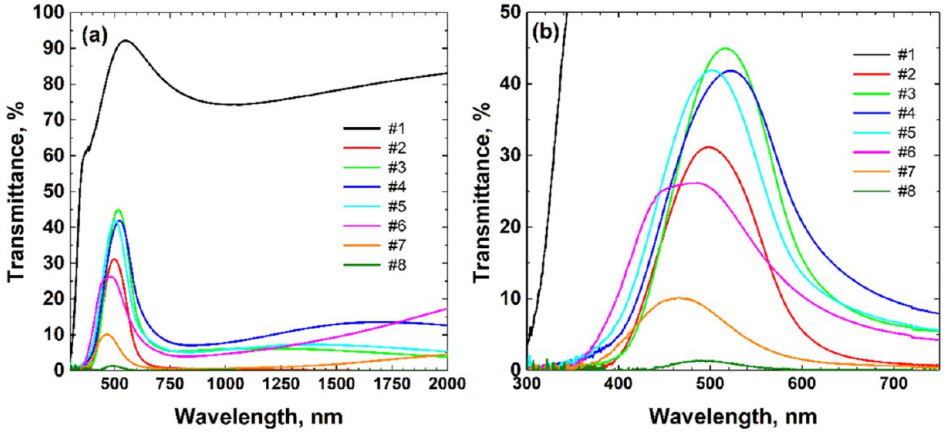

Figure 3. (a) Optical transmission spectra of the thin-film samples and (b) zoom-in view of the same spectra in regions 300−750 nm. Note that all samples have different thicknesses.

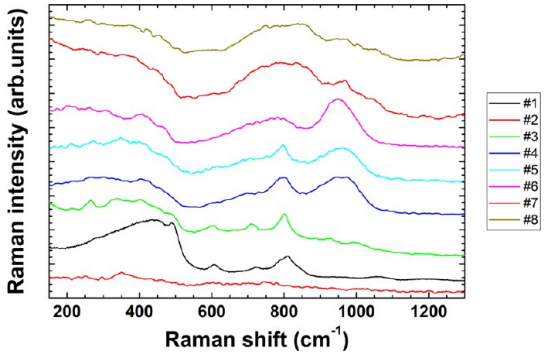

Figure 4. Raman scattering spectra of WO_3−ReO_3 thin-film samples excited by a laser with the wavelength of 532 nm at the power of 0.46 mW.

Moreover, the XRD patterns of samples produced using the same technology inref 41 were qualitatively interpreted to be due to cubic or orthorhombic tungsten oxide phases, but again not all peaks in the XRD pattern of the cubic c-WO_3 phase were assigned. At the same time, the cubic c-WO_3 sample synthesized at high pressure and temperature inref 42 demonstrates good quality XRD pattern refined in space group $Pm\bar{3}m$ but its Raman spectrum is different from that inref 40 and our spectra in Figure 3a. Thus, the origin of the band at 950 cm^{-1} in our samples is still obscure.

The correlation between the 950 cm^{-1} band intensity and the amount of tungsten in WO_3−ReO_3 solid solutions allows us to assume that the band is related to the tungsten sublattice. Note that the W−O phonon modes with large (>900 cm^{-1}) wavenumber values exist in all pure WO_3 phases but they are not Raman active.[28] Therefore, we propose that an increase of the unit cell and the presence of rhenium ions in the solid solutions may lead to the activation of new Raman modes.

X-ray Photoelectron Spectroscopy. An XPS study was performed to qualitatively determine the composition of the surface of the thin film and analyze the oxidation states of the Re and W ions. High-resolution spectra of the Re 4f and W 4f peaks were acquired for each sample (Figure 5). The XPS spectrum of sample #1 shows the presence of the W signal: a doublet of 4f7/2 and 4f5/2 at the binding energies of 35.8 and 37.6 eV due to the spin−orbit splitting indicates the presence of W^{6+} in the film. The spectrum of sample #2 (quartz/WO_x/ReO_x annealed at 300 °C) exhibits only the Re signal (Figure 5b), which is present in two oxidation states: Re doublet 4f 7/2 and 4f 5/2 peak energies at binding energies of 43.5 and 46.0 eV correspond to the 6+ and 7+ oxidation states, respectively, indicating the presence of ReO_3 and Re_2O_7 compounds on the surface of the film.[3,43,44] Sample #3 (quartz/WO_x/ReO_x annealed at 450 °C) has signals from both Re and W (Figure 5c): the spectrum of rhenium is similar to the previous sample. The spectrum of W indicates the presence of W^{6+} in the film.[45,46] The spectra of the samples #4 and #5 (quartz/c-ReO_x/WO_x and quartz/a-ReO_x/WO_x annealed at 450 °C) are almost identical (Figure 5d,e): a strong signal of W 4f doublet peaks characteristic for W^{6+} and a weak signal of Re 4f doublet peaks for Re^{7+} are visible. Sample #6 (mixed WO_x−ReO_x annealed at 450 °C, Re/W ratio 1:7) also demonstrates a strong signal of W 4f doublet for W^{6+} and a weak signal of Re 4f doublet for Re^{7+} and Re^{6+} (Figure 5f). The spectra of the samples #7 and #8 (mixed WO_x−ReO_x annealed at 450 °C, Re/W ratio 1:2 and 3:1, respectively) also demonstrate strong signals of Re 4f doublets for Re^{7+} and Re^{6+} and W 4f doublet for W^{6+} and W^{5+} (Figure 5g,h).[45,47] The presence of the Re^{7+} signal on the surface of samples #4 and #5 confirms that Re atoms sublime from the bottom Re layer and diffuse through the W layer to the sample surface.

Electrical Properties. Macroscopic electrical resistivity of the WO_3−ReO_3 films was measured at room temperature in the van der Pauw configuration using a Hall measurement system. Current−voltage characteristics were linear for all samples, indicating good ohmic contacts. The resistivity of samples #1 and #6 was too high to be measured by our Hall measurement system. The obtained data are summarized in Table 1. Note, that samples #2, #3, #4, #5 consist of two layers (ReO_3 and WO_3), and conductivity is due to mainly the ReO_3 layer. The minimal resistivity was demonstrated by sample #2 (WO_3/ReO_3 sample heated at 300 °C), where ReO_3 is the upper layer, and the annealing temperature is optimal for the crystallization of ReO_3. However, this temperature is not high enough for the crystallization of WO_3 (see XRD spectrum in Figure 1). The resistivity of sample #3 (WO_3/ReO_3 sample heated at 450 °C) is significantly higher in comparison to sample #2 due to partial sublimation of ReO_3. Samples #4 and #5 (ReO_3/WO_3 heated at 450 °C) have comparable resistivity; however, sample #5 is two times more conductive than #4. Samples #6, #7, and #8 were prepared by simultaneous deposition of rhenium and tungsten oxides and annealed at 450 °C; resistivity of these samples is reversely dependent on rhenium content and is equal to 0.7 Ωm for sample #7 and 7 × 10^{-2} Ωm for sample #8 (resistivity of

https://doi.org/10.1021/acsomega.1c05085
ACS Omega 2022, 7, 1827−1837

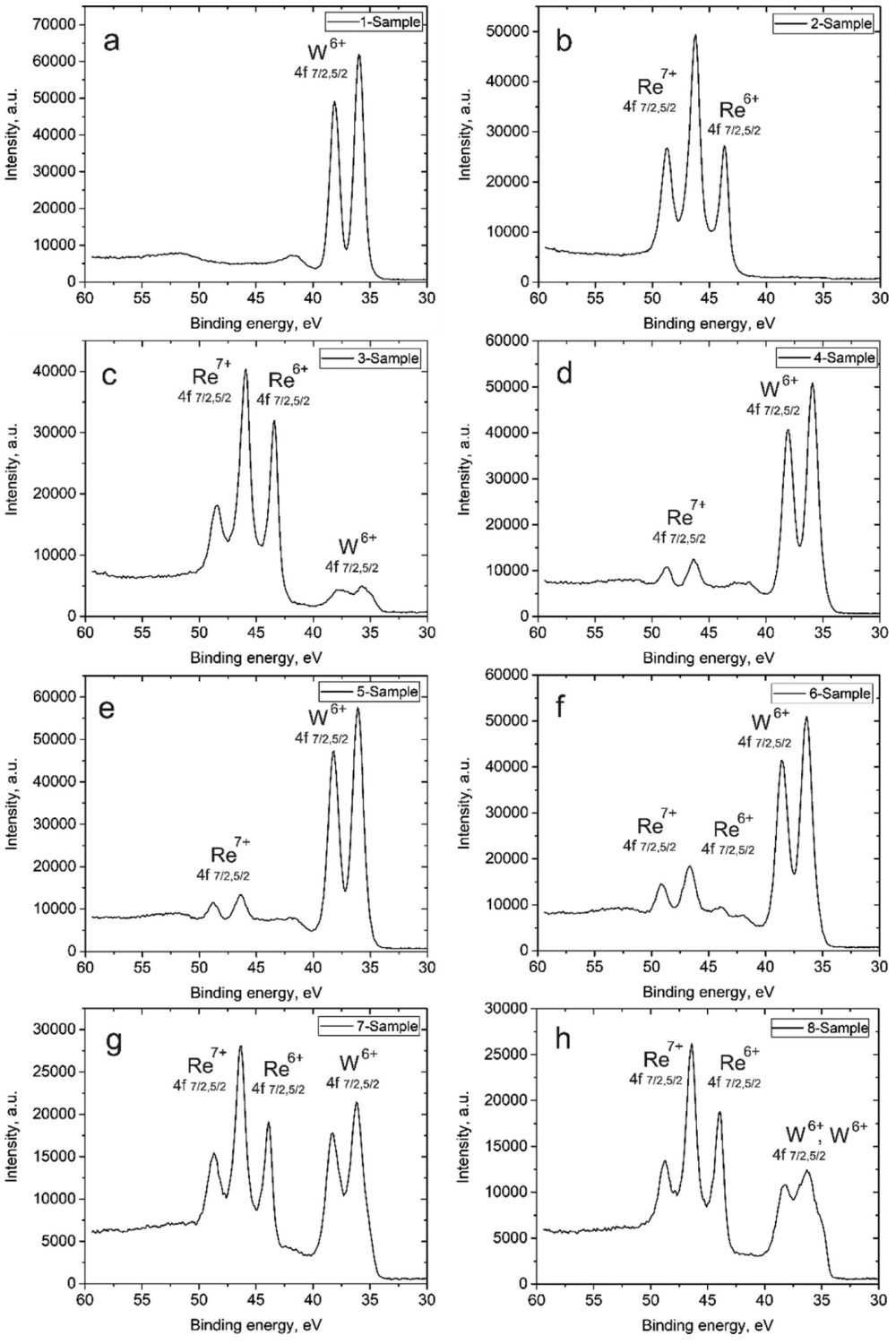

Figure 5. XPS spectra for sample #1 (a), sample #2 (b), sample #3 (c), sample #4 (d), sample #5 (e), sample #6 (f), sample #7 (g), and sample #7 (h).

sample #6 was too high to be measured by our system). The only available data on ReO_3−WO_3 solid solutions resistivity was published by Sleight and Gillson,[11] who reported the electrical resistivity of ReO_3−$3WO_3$ bulk crystals equal to 3.4×10^{-5} Ωm, while the electrical resistivity of pure ReO_3 bulk crystals 3.6×10^{-7} to 8×10^{-8} Ωm depending on the synthesis method.[11] In our previous work,[3] we found minimal electrical resistivity of pure ReO_3 thin films prepared at 250 °C equal to 4.0×10^{-7} Ωm with the tendency to increase at a higher annealing temperature to 1.3×10^{-5} Ωm at 350 °C. In this work, we use an annealing temperature of 450° C to achieve ReO_3−WO_3 film crystallization, which was impossible at 250 and 350 °C.

Conductive AFM. All samples were investigated using conductive AFM to study the electrical properties at a microscopic scale. Sample #1 or pure WO_3 thin film has a very high electrical resistance of 3.8×10^{11} Ω (Figure 6b). Sample #3 having the WO_3 bottom layer and the ReO_3 upper layer demonstrates a lower resistance of 4×10^6 Ω (Figure 6d).

https://doi.org/10.1021/acsomega.1c05085
ACS Omega 2022, 7, 1827−1837

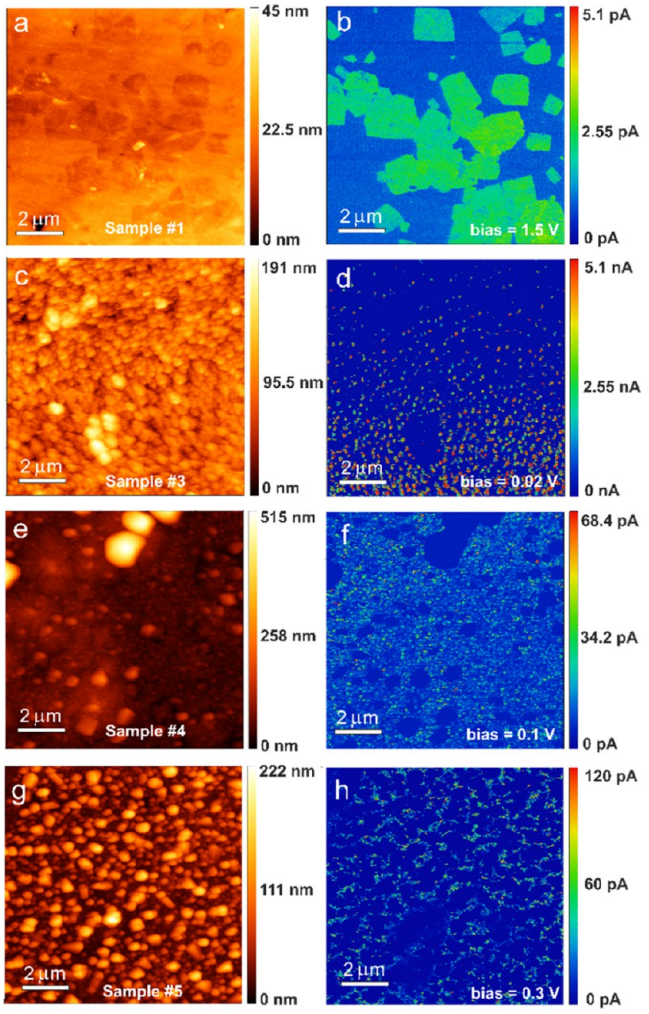

Figure 6. Conductive AFM measurements of sample #1 (a—topography, b—current map), sample #3 (c—topography, d—current map), sample #4 (e—topography, f—current map), and sample #5 (g—topography, h—current map). All samples were annealed for 0.5 h at 450 °C. Note different bias voltages and current ranges for all samples.

Samples #4 and #5 have the ReO_3 bottom layer and the WO_3 upper layer and show high resistance values of 1.6×10^9 Ω and 2.5×10^9 Ω, respectively (Figure 6f,h). The resistance of samples #4 and #5 is significantly lower (at least 2 orders of magnitude) in comparison to sample #1. We suggest rhenium oxide diffusion from the bottom of the ReO_3 layer through the upper WO_3 layer. XPS spectroscopy and tomography data confirm this hypothesis.

Mixed ReO_3–WO_3 samples #6, #7, and #8 show resistance higher than that of sample #3 (having an upper ReO_3 layer) and lower in comparison to samples #4 and #5 (having an upper WO_3 layer): 1.5×10^8, 1.1×10^7, and 1×10^7 Ω, respectively (Figure 7). In other words, the resistivity of mixed ReO_3-WO_3 samples is in between WO_3 and ReO_3 film resistivity. The conductivity map of mixed ReO_3–WO_3 samples demonstrates good homogeneity with the inclusion of small non-conductive regions (discussed later).

SEM Analysis. The surface morphology was studied using SEM. Randomly oriented closely packed ReO_3 crystallites of submicrometer size are visible on the surface of sample #2 (Figure 8a). ReO_3 crystallites are not closely packed on the

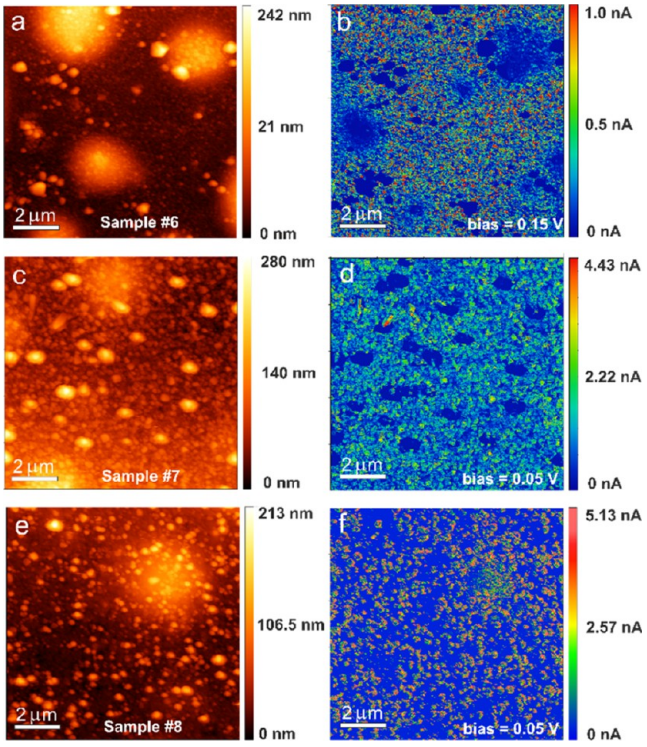

Figure 7. Conductive AFM measurements of sample #6 (a—topography, b—current map), sample #7 (c—topography, d—current map), and sample #8 (e—topography, f—current map). All samples were annealed for 0.5 h at 450 °C. Note different bias voltages and current ranges for all samples.

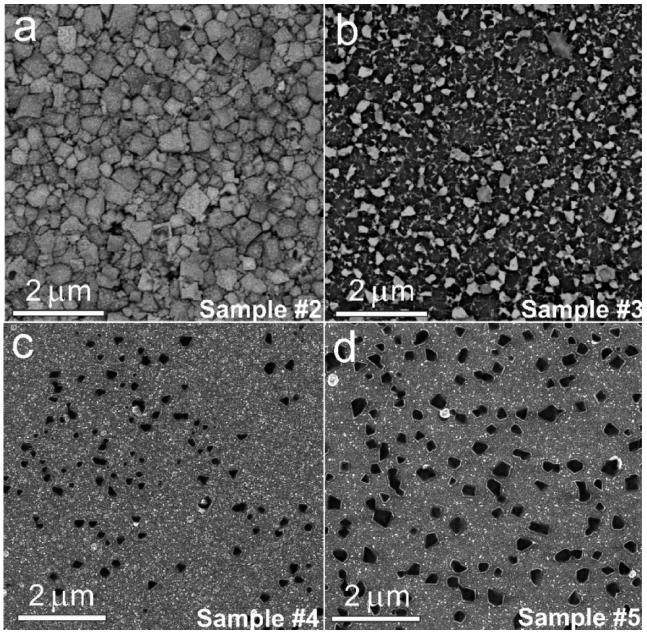

Figure 8. SEM images of sample #2 (a), sample #3 (b), sample #4 (c), and sample #5 (d).

surface of sample #3, probably due to the partial sublimation of the ReO_3 material (Figure 8b). The surface of samples #4 and #5 looks very close, showing a nanocrystalline surface with some arbitrarily shaped crystallites of submicrometer size.

SEM images of mixed WO_3 and ReO_3 thin film samples #6, #7, and #8 are shown in Figure 9. The surface of sample #6 is

https://doi.org/10.1021/acsomega.1c05085
ACS Omega 2022, 7, 1827−1837

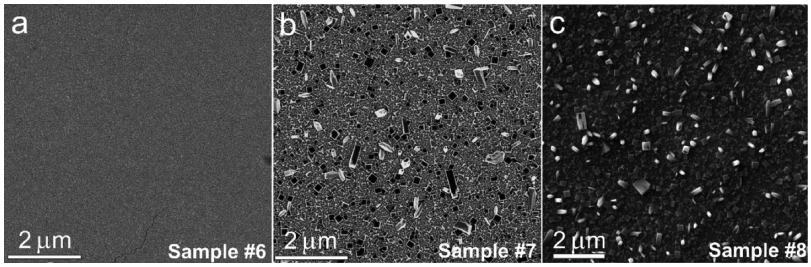

Figure 9. SEM images of sample #6 (a), sample #7 (b), and sample #8 (c).

smooth and featureless, while samples #7 and #8 demonstrate similar small rectangular-shaped crystals.

There are three types of microcrystals visible on AFM and SEM images. First one is pure ReO_3 microcrystals with an arbitrary shape, as shown in Figure 8a,b (can be seen on sample #2 and #3). On the surface of pure ReO_3 thin films annealed at 250−300 °C, these microcrystals have a cubic shape,[3] but at a higher annealing temperature, the shape changes due to sublimation. The second type of crystals are nonconductive and can be seen in AFM images: Figures 6c−h and 7a−d. In SEM images, these microcrystals appear as black crystals, Figure 8c,d. We believe that these are $HReO_4$ crystals, which appear at the ReO_3 containing surface upon exposure to humid air.[48] $HReO_4$ crystals are insulating and not very reactive with atmospheric gases.[48] The third type—hypothetical $Re_xW_{1-x}O_3$ microcrystals—which appears on the surface of mixed samples #6, #7, and #8 is rectangular parallelepiped. All these microcrystals are shown in Figures S5.4, S5.5, and S5.6 of the Supporting Information.

First-Principles DFT Calculations. The results of the first-principles calculations performed within a 2 × 2 × 2 supercell model with removed symmetry and full relaxation of the lattice constants and atomic fractional coordinates are shown in Figure 10 for selected $Re_xW_{1-x}O_3$ solid solutions, which cover the full range of compositions studied experimentally. While our model is rather simple, it predicts the behavior of the cubic ReO_3 structure upon substitution of rhenium atoms with tungsten ones. For all studied compositions, the Fermi level is located in the conduction band, suggesting their metallic conductivity. The bottom of the conduction band is mainly due to the 5d(t_{2g})-states of rhenium and tungsten ions, and the conduction band becomes broadened for the low tungsten content.

In pure WO_3, the conduction band is separated from the valence band by a gap, whose size depends on the oxide phase. Our calculations (Figure S6) suggest that the band gap increases from about 2.3 eV in cubic WO_3 ($Pm\bar{3}m$) to 3.7 eV in orthorhombic ($Pcnb$) and 4.1 eV in triclinic ($P\bar{1}$) WO_3 phases. These results are in good qualitative agreement with previous theoretical studies.[26−28] In solid solutions with a high tungsten content ($Re_{0.125}W_{0.875}O_3$), the calculations predict a separation (a gap) of about 2.2 eV between the top of the 2p(O) states and the bottom of 5d(Re/W)-states. Upon increasing the rhenium concentration, this gap decreases down to about 0.6 eV in $Re_{0.875}W_{0.125}O_3$ and is equal to 0.4 eV for pure cubic ReO_3. Thus, the value of the gap between the 2p(O) and 5d(Re/W)-states in $Re_xW_{1-x}O_3$ solid solutions is between that for pure WO_3 and ReO_3 phases. The Mulliken population analysis indicates that the charges on tungsten and rhenium ions decrease slightly from Z(Re) = +2.76 and Z(W) = +2.81 in $Re_{0.125}W_{0.875}O_3$ to Z(Re) = +2.70 and Z(W) = +2.77 in $Re_{0.875}W_{0.125}O_3$ as a result of electron delocalization.

The most intriguing result of our calculations is the strong evidence of the supercell tetragonal distortion occurring upon an increase of the tungsten content (Table S1), which is also found by the Rietveld refinement of the experimental diffraction patterns (Figure 1 and Table S2). At a large rhenium concentration ($Re_{0.875}W_{0.125}O_3$), the shape of the supercell is cubic, and both rhenium and tungsten ions are located within the regular octahedra. The W−O bond length is slightly longer (by 0.02 Å) than that of Re−O. However, already in $Re_{0.75}W_{0.25}O_3$, the early evidence of the tetragonal distortion starts to appear as slightly non-equivalent Re−O bond lengths. In $Re_{0.5}W_{0.5}O_3$ solid solution, the difference between a, b, and c lattice parameters and the axial distortion of the WO_6 and ReO_6 octahedra is well observed and indicates the tetragonal distortion of the lattice. At lower rhenium concentration ($Re_{0.25}W_{0.75}O_3$), the lattice distortion increases further, promoting the rotation of the metal−oxygen octahedra and off-center displacements of metal ions (Figure 10). The tetragonality of the lattice is well reflected in the lattice parameters with c being larger than a and b. Thus, our first-principles DFT calculations suggest that the addition of tungsten to ReO_3 induces the tetragonal distortion of the lattice in agreement with the XRD results discussed above.

CONCLUSIONS

In this work, we produced layered WO_3/ReO_3, ReO_3/WO_3 and mixed ReO_3−WO_3 thin films by reactive DC magnetron sputtering and subsequent annealing in air. In contrast to previously reported methods, our synthesis method benefits from high flexibility in the Re-to-W ratio in the resulting material, allowing high Re content (>50%) at moderate temperatures and without the use of high pressure. The possibility to vary Re content over a wide range opens a route for tweaking and fine tuning the properties of ReO_3−WO_3 to meet the needs of potential applications.

Separate cubic ReO_3 ($Pm\bar{3}m$) and monoclinic WO_3 ($P2_1/n$) phases were found by Rietveld refinement of XRD patterns in layered thin films; WO_3/ReO_3 (sample #3) and ReO_3/WO_3 (sample #4) were annealed at 450 °C. However, the tetragonal ($P4/nmm$) phase was revealed in layered ReO_3/WO_3 (sample #5) and mixed ReO_3−WO_3 films (samples #6, #7, #8), which possibly indicates the formation of $Re_xW_{1-x}O_3$ solid solutions.

Conductive AFM measurements confirm rhenium oxide diffusion through the WO_3 layer during annealing (samples #4 and #5). Macroscopic electrical measurements and conductive AFM show correlation of film conductivity with the increase of Re content in mixed ReO_3−WO_3 thin films.

First-principles DFT calculations were performed for selected compositions of $Re_xW_{1-x}O_3$ solid solutions to predict their crystallographic phase and electronic properties. The calculations suggest that $Re_xW_{1-x}O_3$ solid solutions possess electrical

https://doi.org/10.1021/acsomega.1c05085
ACS Omega 2022, 7, 1827−1837

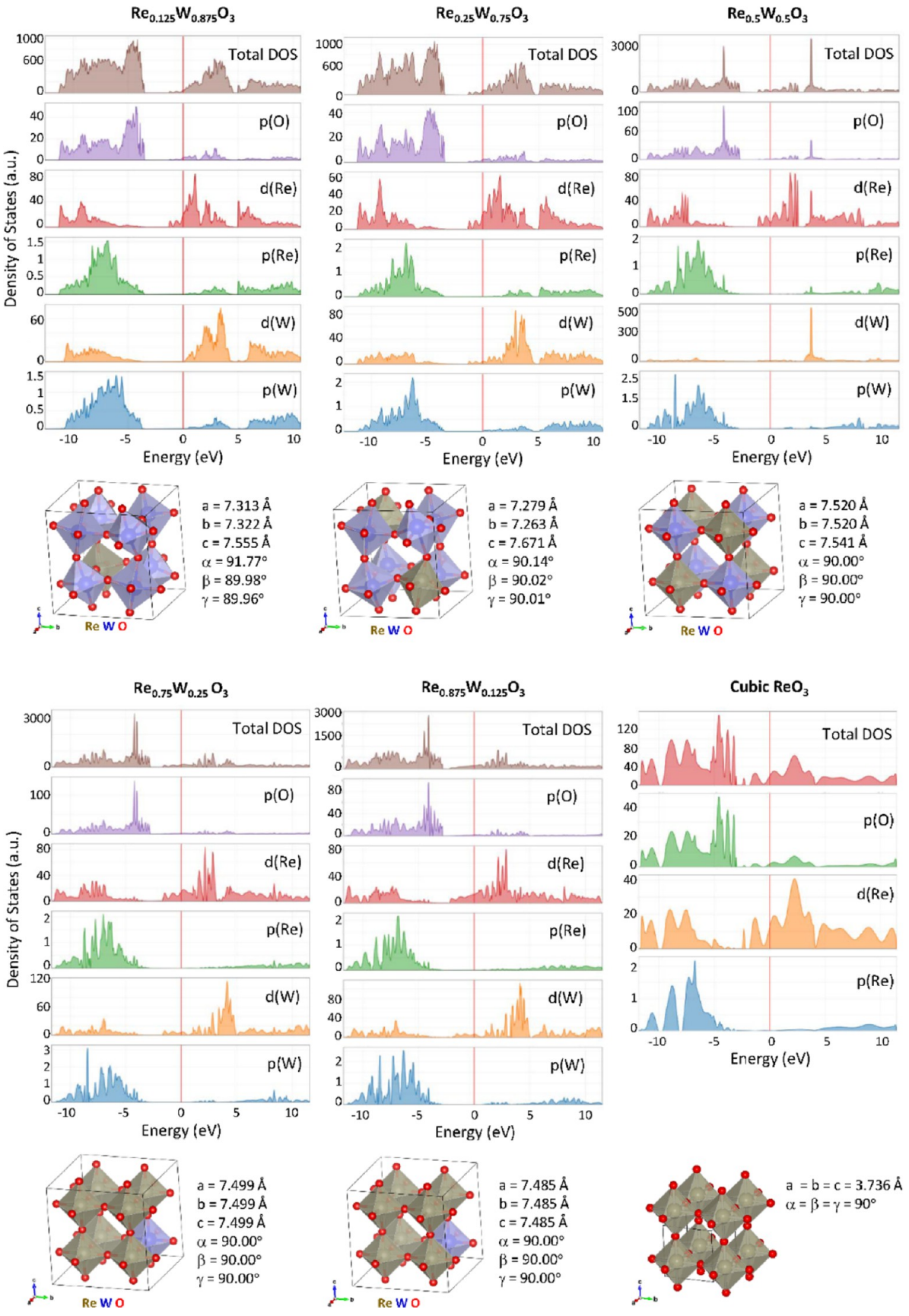

Figure 10. Total and projected densities of states (DOSs) of the set of atomic orbitals for the four selected models of $Re_xW_{1-x}O_3$ solid solutions and pure ReO_3 for comparison. The energy zero is set at the Fermi level E_F. The supercells used in the calculations are shown at the bottom, and lattice parameters are shown for each model.

https://doi.org/10.1021/acsomega.1c05085
ACS Omega 2022, 7, 1827−1837

conductivity, which was confirmed by microscopic and macroscopic electrical measurements. Moreover, our DFT calculations predict that the addition of tungsten to ReO_3 induces tetragonal distortion of the lattice in agreement with the XRD results.

The new synthesis method of crystalline layered ReO_3/WO_3 and mixed ReO_3–WO_3 thin films opens the door for further studies.

■ ASSOCIATED CONTENT

Supporting Information

The Supporting Information is available free of charge at https://pubs.acs.org/doi/10.1021/acsomega.1c05085.

Detailed description of sample characterization, first-principles DFT calculations and data, visual appearance of the samples, transmittance spectrum of the pure ReO_3 thin film, TEM images, high-magnification AFM images, and high-magnification SEM images (PDF)

■ AUTHOR INFORMATION

Corresponding Author

Boris Polyakov – *Institute of Solid State Physics, University of Latvia, LV-1063 Riga, Latvia;* orcid.org/0000-0002-6626-1065; Email: boris.polyakov@cfi.lu.lv

Authors

Edgars Butanovs – *Institute of Solid State Physics, University of Latvia, LV-1063 Riga, Latvia;* orcid.org/0000-0003-3796-1190

Andrejs Ogurcovs – *Institute of Solid State Physics, University of Latvia, LV-1063 Riga, Latvia*

Anatolijs Sarakovskis – *Institute of Solid State Physics, University of Latvia, LV-1063 Riga, Latvia*

Martins Zubkins – *Institute of Solid State Physics, University of Latvia, LV-1063 Riga, Latvia*

Liga Bikse – *Institute of Solid State Physics, University of Latvia, LV-1063 Riga, Latvia*

Jevgenijs Gabrusenoks – *Institute of Solid State Physics, University of Latvia, LV-1063 Riga, Latvia*

Sergei Vlassov – *Institute of Physics, University of Tartu, 50412 Tartu, Estonia*

Alexei Kuzmin – *Institute of Solid State Physics, University of Latvia, LV-1063 Riga, Latvia;* orcid.org/0000-0003-4641-6354

Juris Purans – *Institute of Solid State Physics, University of Latvia, LV-1063 Riga, Latvia*

Complete contact information is available at: https://pubs.acs.org/10.1021/acsomega.1c05085

Notes

The authors declare no competing financial interest.

■ ACKNOWLEDGMENTS

The financial support was provided by ERAF Project Nr. 1.1.1.1/18/A/073. The Institute of Solid State Physics, University of Latvia (Latvia) as the Centre of Excellence has received funding from the European Union's Horizon 2020 Framework Programme H2020-WIDESPREAD01-2016-2017-Teaming Phase2 under grant agreement no. 739508, project CAMART2.

■ REFERENCES

(1) Bashian, N. H.; Zhou, S.; Zuba, M.; Ganose, A. M.; Stiles, J. W.; Ee, A.; Ashby, D. S.; Scanlon, D. O.; Piper, L. F. J.; Dunn, B.; Melot, B. C. Correlated Polyhedral Rotations in the Absence of Polarons during Electrochemical Insertion of Lithium in ReO $_3$. *ACS Energy Lett.* **2018**, *3*, 2513−2519.

(2) King, C. N.; Kirsch, H. C.; Geballe, T. H. The Low Temperature Heat Capacity and Electrical Resistivity of ReO3. *Solid State Commun.* **1971**, *9*, 907−910.

(3) Polyakov, B.; Butanovs, E.; Ogurcovs, A.; Vlassov, S.; Zubkins, M.; Jonane, I.; Cintins, A.; Kalinko, A.; Kuzmin, A.; Purans, J. Understanding the Conversion Process of Magnetron-Deposited Thin Films of Amorphous ReOx to Crystalline ReO3 upon Thermal Annealing. *Cryst. Growth Des.* **2020**, *20*, 6147−6156.

(4) Shigeo, N. *Handbook of Heterogeneous Catalytic Hydrogenation for Organic Synthesis*; Wiley-Interscience: New York, 2001.

(5) Wang, F.; DiValentin, C.; Pacchioni, G. Rational Band Gap Engineering of WO3 Photocatalyst for Visible Light Water Splitting. *ChemCatChem* **2012**, *4*, 476−478.

(6) Lee, W. J.; Fang, Y. K.; Ho, J.-J.; Hsieh, W. T.; Ting, S. F.; Huang, D.; Ho, F. C. Effects of Surface Porosity on Tungsten Trioxide(WO3) Films' Electrochromic Performance. *J. Electron. Mater.* **2000**, *29*, 183−187.

(7) Jiménez, I.; Arbiol, J.; Dezanneau, G.; Cornet, A.; Morante, J. R. Crystalline Structure, Defects and Gas Sensor Response to NO2 and H2S of Tungsten Trioxide Nanopowders. *Sens. Actuators, B* **2003**, *93*, 475−485.

(8) Shannon, R. D. Revised Effective Ionic Radii and Systematic Studies of Interatomic Distances in Halides and Chalcogenides. *Acta Crystallogr., Sect. A: Found. Adv.* **1976**, *32*, 751−767.

(9) Ling, S.; Mei, D.; Gutowski, M. Reactivity of Hydrogen and Methanol on (001) Surfaces of WO3, ReO3, WO3/ReO3 and ReO3/WO3. *Catal. Today* **2011**, *165*, 41−48.

(10) Schick, J. T.; Jiang, L.; Saldana-Greco, D.; Rappe, A. M. Coupling between Octahedral Rotations and Local Polar Displacements in W O 3 / Re O 3 Superlattices. *Phys. Rev. B: Condens. Matter Mater. Phys.* **2014**, *89*, 195304.

(11) Sleight, A. W.; Gillson, J. L. Preparation and Properties of Alkali Rhenium Bronzes and a WO3 - ReO3 Solid Solution. *Solid State Commun.* **1966**, *4*, 601−602.

(12) Helbig, C.; Herrmann, R.; Mayr, F.; Scheidt, E.-W.; Tröster, K.; Hanss, J.; von Nidda, H.-A. K.; Heymann, G.; Huppertz, H.; Scherer, W. An Organometallic Chimie Douce Approach to New RexW1−XO3 Phases. *Chem. Commun.* **2005**, *32*, 4071.

(13) Taut, T.; Kleeberg, R.; Bergmann, J. *Seifert Software: The New Seifert Rietveld Program Bgmn and Its Application to Quantitative Phase Analysis.* 1998.

(14) Doebelin, N.; Kleeberg, R. Profex: A Graphical User Interface for the Rietveld Refinement Program BGMN. *J. Appl. Crystallogr.* **2015**, *48*, 1573−1580.

(15) Dovesi, R.; Saunders, V. R.; Roetti, C.; Orlando, R.; Zicovich-Wilson, C. M.; Pascale, F.; Civalleri, B.; Doll, K.; Causà, N. M. H.; Bush, I. J., D'Arco, P.; Llunell, M. M.; Noël, Y. *CRYSTAL14 User's Manual*; University of Torino: Torino, 2014.

(16) Evarestov, R. A.; Kalinko, A.; Kuzmin, A.; Losev, M.; Purans, J. First-Principles Lcao Calculations on 5d Transition Metal Oxides: Electronic and Phonon Properties. *Integr. Ferroelectr.* **2009**, *108*, 1−10.

(17) Vilela Oliveira, D.; Laun, J.; Peintinger, M. F.; Bredow, T. BSSE-correction scheme for consistent gaussian basis sets of double- and triple-zeta valence with polarization quality for solid-state calculations. *J. Comput. Chem.* **2019**, *40*, 2364−2376.

(18) Monkhorst, H. J.; Pack, J. D. Special Points for Brillouin-Zone Integrations. *Phys. Rev. B: Solid State* **1976**, *13*, 5188−5192.

(19) Zhao, Y.; Truhlar, D. G. The M06 Suite of Density Functionals for Main Group Thermochemistry, Thermochemical Kinetics, Noncovalent Interactions, Excited States, and Transition Elements: Two New Functionals and Systematic Testing of Four M06-Class Functionals and 12 Other Functionals. *Theor. Chem. Acc.* **2008**, *120*, 215−241.

(20) Jørgensen, J.-E.; Staun Olsen, J.; Gerward, L. Phase Transitions in ReO3 Studied by High-Pressure X-Ray Diffraction. *J. Appl. Crystallogr.* **2000**, *33*, 279−284.
(21) Mulliken, R. S. Electronic Population Analysis on LCAO−MO Molecular Wave Functions. I. *J. Chem. Phys.* **1955**, *23*, 1833−1840.
(22) Locherer, K. R.; Swainson, I. P.; Salje, E. K. H. Phase Transitions in Tungsten Trioxide at High Temperatures - a New Look. *J. Phys.: Condens. Matter* **1999**, *11*, 6737−6756.
(23) Vogt, T.; Woodward, P. M.; Hunter, B. A. The High-Temperature Phases of WO3. *J. Solid State Chem.* **1999**, *144*, 209−215.
(24) Howard, C. J.; Luca, V.; Knight, K. S. High-Temperature Phase Transitions in Tungsten Trioxide - the Last Word? *J. Phys.: Condens. Matter* **2001**, *14*, 377−387.
(25) Corà, F.; Stachiotti, M. G.; Catlow, C. R. A.; Rodriguez, C. O. Transition Metal Oxide Chemistry:Electronic Structure Study of WO3 ,ReO3 ,and NaWO3. *J. Phys. Chem. B* **1997**, *101*, 3945−3952.
(26) Wang, F.; Di Valentin, C.; Pacchioni, G. Electronic and Structural Properties of WO3: A Systematic Hybrid DFT Study. *J. Phys. Chem. C* **2011**, *115*, 8345−8353.
(27) Hamdi, H.; Salje, E. K. H.; Ghosez, P.; Bousquet, E. First-Principles Reinvestigation of Bulk WO3. *Phys. Rev. B* **2016**, *94*, 245124.
(28) Yang, H.; Sun, H.; Li, Q.; Li, P.; Song, K.; Song, B.; Wang, L. Structural, Electronic, Optical and Lattice Dynamic Properties of the Different WO3 Phases: First-Principle Calculation. *Vacuum* **2019**, *164*, 411−420.
(29) Guillén, C.; Herrero, J. Amorphous WO3-x Thin Films with Color Characteristics Tuned by the Oxygen Vacancies Created during Reactive DC Sputtering. *J. Mater. Sci. Technol.* **2021**, *78*, 223−228.
(30) Zhao, Y.; Zhang, X.; Chen, X.; Li, W.; Wang, L.; Ren, F.; Zhao, J.; Endres, F.; Li, Y. Preparation of WO3 Films with Controllable Crystallinity for Improved Near-Infrared Electrochromic Performances. *ACS Sustainable Chem. Eng.* **2020**, *8*, 11658−11666.
(31) Salje, E. Lattice Dynamics of WO3. *Acta Crystallogr., Sect. A: Found. Adv.* **1975**, *31*, 360−363.
(32) Cazzanelli, E.; Vinegoni, C.; Mariotto, G.; Kuzmin, A.; Purans, J. Low-Temperature Polymorphism in Tungsten Trioxide Powders and Its Dependence on Mechanical Treatments. *J. Solid State Chem.* **1999**, *143*, 24−32.
(33) Purans, J.; Kuzmin, A.; Cazzanelli, E.; Mariotto, G. Disorder-Induced Raman Scattering in Rhenium Trioxide (ReO3). *J. Phys.: Condens. Matter* **2007**, *19*, 226206.
(34) Daniel, M. F.; Desbat, B.; Lassegues, J. C.; Gerand, B.; Figlarz, M. Infrared and Raman Study of WO3 Tungsten Trioxides and WO3, XH2O Tungsten Trioxide Tydrates. *J. Solid State Chem.* **1987**, *67*, 235−247.
(35) Ramāns, G. M.; Gabrusenoks, J. V.; Veispāls, A. A. Structure of Tungstic Acids and Amorphous and Crystalline WO3 Thin Films. *Phys. Status Solidi A* **1982**, *74*, K41−K44.
(36) Thi, M.; Velasco, G. Raman Study of WO3 Thin Films. *Solid State Ionics* **1984**, *14*, 217−220.
(37) Lee, S.-H.; Cheong, H. M.; Zhang, J.-G.; Mascarenhas, A.; Benson, D. K.; Deb, S. K. Electrochromic Mechanism in A-WO3−y Thin Films. *Appl. Phys. Lett.* **1999**, *74*, 242−244.
(38) Boulova, M.; Gaskov, A.; Lucazeau, G. Tungsten Oxide Reactivity versus CH4, CO and NO2 Molecules Studied by Raman Spectroscopy. *Sens. Actuators, B* **2001**, *81*, 99−106.
(39) Kuzmin, A.; Purans, J.; Cazzanelli, E.; Vinegoni, C.; Mariotto, G. X-Ray Diffraction, Extended x-Ray Absorption Fine Structure and Raman Spectroscopy Studies of WO3 Powders and (1−x)WO3−y·xReO2 Mixtures. *J. Appl. Phys.* **1998**, *84*, 5515−5524.
(40) Kustova, G. N.; Chesalov, Y. A.; Plyasova, L. M.; Molina, I. Y.; Nizovskii, A. I. Vibrational Spectra of WO3·nH2O and WO3 Polymorphs. *Vib. Spectrosc.* **2011**, *55*, 235−240.
(41) Balázsi, C.; Farkas-Jahnke, M.; Kotsis, I.; Petrás, L.; Pfeifer, J. The Observation of Cubic Tungsten Trioxide at High-Temperature Dehydration of Tungstic Acid Hydrate. *Solid State Ionics* **2001**, *141−142*, 411−416.
(42) Crichton, W. A.; Bouvier, P.; Grzechnik, A. The First Bulk Synthesis of ReO3-Type Tungsten Trioxide, WO3, from Nanometric Precursors. *Mater. Res. Bull.* **2003**, *38*, 289−296.
(43) Greiner, M. T.; Rocha, T. C. R.; Johnson, B.; Klyushin, A.; Knop-Gericke, A.; Schlögl, R. The Oxidation of Rhenium and Identification of Rhenium Oxides During Catalytic Partial Oxidation of Ethylene: An In-Situ XPS Study. *Z. Phys. Chem.* **2014**, *228* (). https://doi.org/DOI: 10.1515/zpch-2014-0002.
(44) Okal, J.; Tylus, W.; Kępiński, L. XPS Study of Oxidation of Rhenium Metal on γ-Al2O3 Support. *J. Catal.* **2004**, *225*, 498−509.
(45) García-García, F. J.; Mosa, J.; González-Elipe, A. R.; Aparicio, M. Sodium Ion Storage Performance of Magnetron Sputtered WO3 Thin Films. *Electrochim. Acta* **2019**, *321*, 134669.
(46) Madhavi, V.; Kondaiah, P.; Hussain, O. M.; Uthanna, S. Electrochemical Properties of Magnetron Sputtered WO3 Thin Films. *AIP Conf. Proc.* **2013**, *1512*, 758−759.
(47) Cui, Y.; Liang, F.; Ji, C.; Xu, S.; Wang, H.; Lin, Z.; Liu, J. Discoloration Effect and One-Step Synthesis of Hydrogen Tungsten and Molybdenum Bronze (HxMO3) using Liquid Metal at Room Temperature. *ACS Omega* **2019**, *4*, 7428−7435.
(48) Cazzanelli, E.; Castriota, M.; Marino, S.; Scaramuzza, N.; Purans, J.; Kuzmin, A.; Kalendarev, R.; Mariotto, G.; Das, G. Characterization of rhenium oxide films and their application to liquid crystal cells. *J. Appl. Phys.* **2009**, *105*, 114904.

https://doi.org/10.1021/acsomega.1c05085
ACS Omega 2022, 7, 1827−1837